Stable and Recyclable Photocatalysts of $CsPbBr_3$@MSNs Nanocomposites for Photoinduced Electron Transfer RAFT Polymerization

Chunyu Zhao,† Haixia Song,† Yinghao Chen,† Wei Xiong,† Mingyou Hu†, Youshen Wu,† Yanfeng Zhang,†, Ling He,† Yi Liu,*,‡, Aizhao Pan*,†*

† Department of Chemistry, School of Chemistry, Xi'an Jiaotong University, Xianning West Road, 28, Xi'an, 710049, China.

‡ The Molecular Foundry and Materials Sciences Division, Lawrence Berkeley National Laboratory, Berkeley, California, 94720, United States.

Corresponding Author

*Email: panaizhao2017032@xjtu.edu.cn.

ABSTRACT: All-inorganic metal halide perovskite $CsPbX_3$ (X = Cl, Br, I) nanocrystals (NCs) have demonstrated attractive optoelectronic characteristics. However, their photocatalytic properties are limited by their poor stability and easy recombination of photogenerated carriers.

Herein, we introduced the $CsPbBr_3$@MSNs nanocomposite ($CsPbBr_3$ NCs embedded in dendritic mesoporous silica nanospheres-MSNs) as photocatalysts for efficient photo-induced electron transfer reversible addition-fragmentation chain transfer (PET-RAFT) polymerization. The $CsPbBr_3$ nanocrystals (~8.1 nm; PLQY of 62±2.1%) were embedded in dendritic MSNs using a nano-confinement strategy. PET-RAFT polymerization was successfully initiated using the $CsPbBr_3$@MSNs nanocomposite as the photocatalyst. Reaction variables such as catalyst loading, monomer composition, and excitation light wavelengths, were varied to yield polymers with desired control of molecular weight and dispersity as well as block copolymers with high chain-end fidelity. In addition, perovskite-based photocatalysts could be readily separated and purified, which allowed effective and rapid recycling of the nanocomposites for multiple polymerization cycles.

TOC GRAPHICS

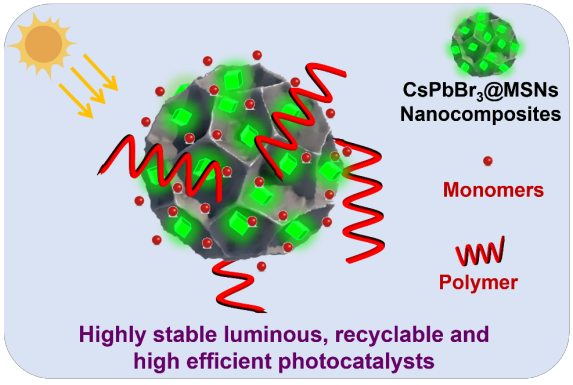

All-inorganic lead halide perovskite $CsPbX_3$ (X = Cl, Br, I) nanocrystals (NCs) have emerged as one of the promising candidates for optoelectronic applications, such as solar cells, light-emitting diodes, photodetectors, and lasers, which inspired growing interests to understand their excellent optoelectronic characteristics[1-5]. Aside from optoelectronic applications, the excellent

charge carrier transport properties, large absorption coefficients and adjustable band gaps render the perovskites as promising photocatalysts for chemical transformations, such as hydrogen generation, organic synthesis, CO_2 reduction, and radical polymerizations.[6-10]

Great interests have been devoted to advance photoinduced reversible-deactivation radical polymerizations (RDRP) for the preparation of macromolecules with multi-architectures, high spatial and temporal resolution, and precise chemical composition under mild reaction conditions.[11-14] Recent efforts in utilizing lead halide perovskite and perovskite−based nanocomposites for photo-driven radical polymerization have demonstrated comparable or superior catalytic properties to the traditional organic photocatalysts, metal complexes, and emerging semiconductors.[15-18] For example, the reductive potentials of excited $CsPbBr_3$ NCs and typical activated reversible addition-fragmentation chain transfer (RAFT) agents were −1.3 V and –0.3 to -0.8 V, respectively (versus a saturated calomel electrode, SCE).[15, 19, 20] The reductive potential of $CsPbBr_3$ was sufficiently negative to activate typical RAFT agents, allowing the transfer of photogenerated electrons from NCs to the RAFT agents to induce RAFT polymerization.[15, 21] Therefore, $CsPbBr_3$ can be a potent photocatalyst for photo-induced electron transfer RAFT (PET-RAFT) polymerization. However, the instability of $CsPbBr_3$ toward ultraviolet (UV) light, heat, and moisture led to NC degradation, PL loss, and poor optoelectronic efficiencies, which prevent its practical applications.[22-25]

To circumvent the inherent issues of perovskite nanocrystals, many approaches have been developed to encapsulate $CsPbX_3$ nanocrystals in protective matrices to improve their chemical and photostability.[22, 26, 27] Examples involve both inorganic constituents (such as Al_2O_3, zeolite-Y, or silica) and polymer matrices (such as polyvinylidene fluoride, polymethylmethacrylate, polystyrene, or tailored block copolymers).[28-31] Among those, porous materials have attracted

particular interests for their ability to host inorganic perovskite nanocrystals inside porous matrices, such as the mesoporous TiO_2 framework, SiO_2 nanospheres (MSNs), and metal−organic frameworks (MOF).[28, 32-34] The fascinating characteristics of facile synthesis, controllable surface functionalization, tunable porous sizes, nontoxicity, and excellent stability render MSNs a promising matrix for hosting the confined growth of perovskite nanocrystals. It is envisioned that the use of MSNs host will not only facilitate the growth of surfactant-free perovskite NCs with controllable sizes and diverse compositions on a larger scale, but also imbue high photostability by effective spatial confinement and separation of the NCs.[35-38]

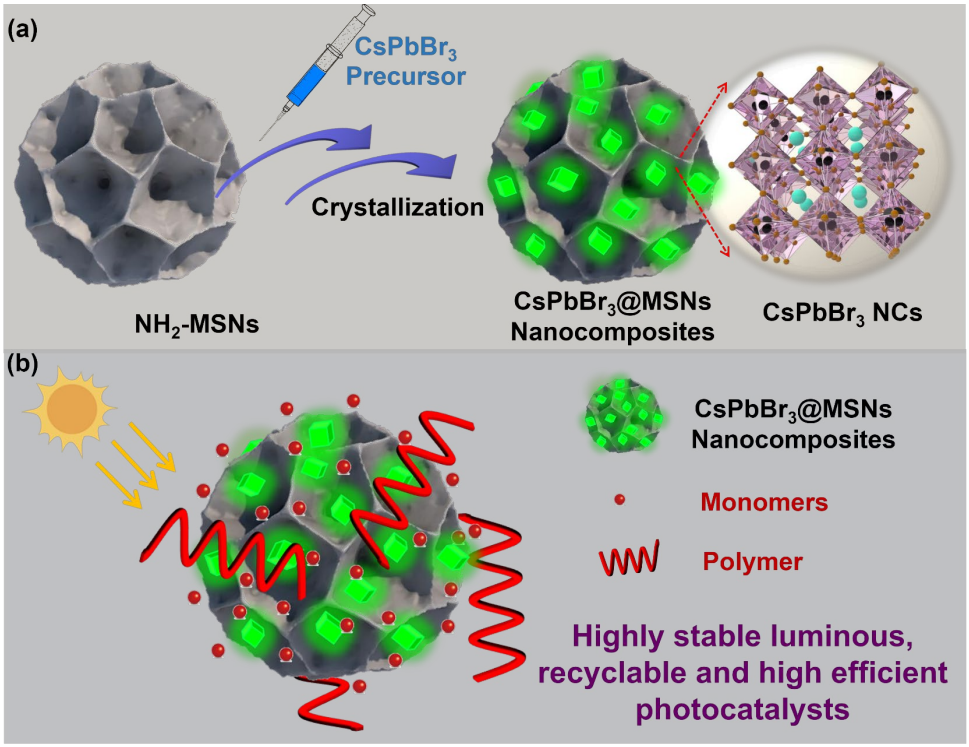

Scheme 1. (a) Schematic illustration of the *in-situ* formation and crystallization strategy of the $CsPbBr_3$@MSNs nanocomposites. (b) Illustration of PET-RAFT polymerization catalyzed by $CsPbBr_3$@MSNs nanocomposites.

Herein, we have explored the use of $CsPbBr_3$@MSNs nanocomposites as the photocatalysts for PET-RAFT polymerization (**Scheme 1**). The $CsPbBr_3$ nanocrystals were grown *in situ* in

dendritic mesoporous silica nanospheres using a nano-confinement strategy.[35, 36] PET-RAFT polymerization was performed with various catalyst loadings, excitation wavelengths, and monomers. The $CsPbBr_3$@MSNs composite has demonstrated excellent catalytic activity and photostability, making it a recyclable photocatalyst for successive PET-RAFT polymerization.

The $CsPbBr_3$@MSNs composites were synthesized following a modified nano-confinement strategy to grow $CsPbBr_3$ nanocrystals encapsulated within dendritic mesoporous silica nanospheres (MSNs) (**Scheme 1a**).[35, 36] Typically, we soaked the amino-modified mesoporous silica nanoparticles (NH_2-MSNs) with a precursor solution of $PbBr_2$ and Cs_2CO_3 in DMSO. Surface amino-functionalized MSNs (NH_2-MSNs) was analyzed by using infrared (IR) and XPS spectroscopy. Compared with the spectrum of MSNs, strong peaks at 2850/2925 cm^{-1} and 1500/1390 cm^{-1} can be clearly observed of NH_2-MSNs, which were ascribed to respective stretching and bending vibrations of $-CH_2-/-CH_3$, respectively. Besides, the stretching vibration of NH_2 groups can be detected at 3300 cm^{-1}. XPS analysis further confirmed that the elemental composition of the final NH_2-MSNs contained all the elements expected from amino groups and MSNs. IR and XPS spectroscopy verified the successful grafting of amino groups on the surface of MSNs (**Figure S1**). The alkylamine on MSNs served as surface ligands and coordinated the perovskite precursors (Pb^{2+} or Cs^{+}) to form nucleation points. The pre-saturated powder was heated at 120 °C for crystallization. A yellow powder was obtained and stored after drying under a vacuum. The production of nanocomposites can be facilely scaled up by proportionally increasing the quantity of precursors, from which the product can be obtained in >2 g scale in one pot (**Figure S2**).

Transmission electron microscopy (TEM) revealed details of the $CsPbBr_3$@MSNs nanocomposite morphologies **(Figure 1)**. For amino-modified MSNs, a uniform spherical profile

with typical center-radial dendritic pore channels (diameter: ~200 nm) was readily observed **(Figure S3)**. Compared with pure NH_2-MSNs, the dendritic pores were filled with black dots, which demonstrated the occupation of the pore space by $CsPbBr_3$ NCs (**Figure 1a**). Similar morphologies were observed at different locations under SEM characterization (**Figure S4**). We performed high-resolution (HR) TEM to confirm the $CsPbBr_3$ NC formation inside the MSNs (**Figure 1b**). The resulting NCs (average diameter ~8 nm) were observed as being uniformly distributed inside the mesoporous SiO_2 channels **(Figure 1b)**. HR-TEM also revealed that the NCs showed lattice spacings of standard $CsPbBr_3$ crystal phases.[1, 39] Furthermore, all elements (O, Si, Cs, Pb, and Br) were readily detected and uniformly dispersed as seen in TEM-EDS elemental mappings, which confirmed $CsPbBr_3$ NCs formation inside the mesoporous silica particles (**Figure 1c**).

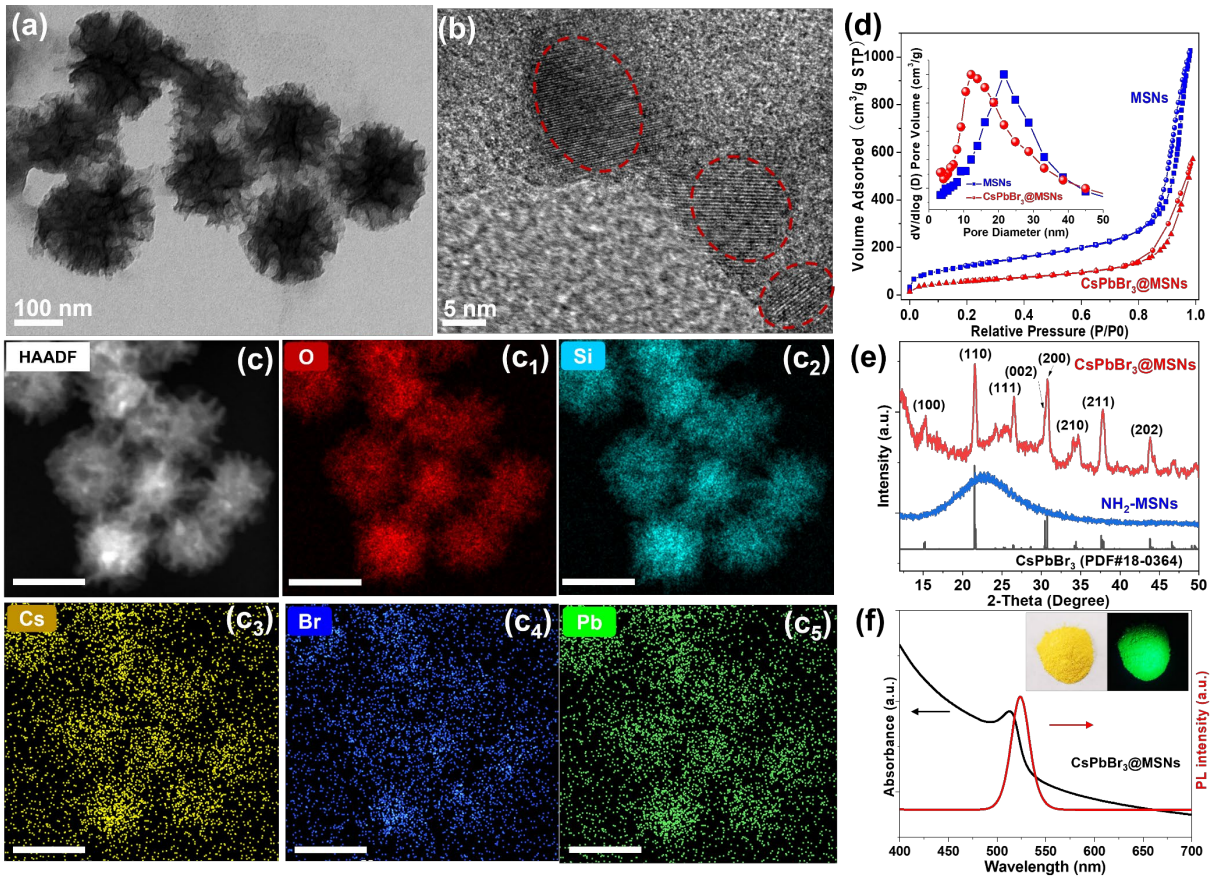

Figure 1. (a) TEM and (b) HR-TEM images of the $CsPbBr_3$@MSNs nanocomposites. (c) TEM elemental mapping profiles for O, Si, Cs, Br, and Pb. (d) N_2 adsorption-desorption isotherms of the MSNs and $CsPbBr_3$@MSNs nanocomposites. Inset in (d) shows the pore size distributions. (e) Powder X-ray diffraction (PXRD) patterns of the $CsPbBr_3$@MSNs nanocomposites and the standard orthorhombic crystal structure of $CsPbBr_3$ (PDF#18-0364). (f) PL and absorption spectra of $CsPbBr_3$@MSNs nanocomposites. Insets in (f) are the optical photographs of bulk $CsPbBr_3$@MSNs powders under visible and UV light.

Furthermore, Brunauer-Emmett-Teller (BET) isotherms **(Figure 1d)** indicated the decrease of pore mouth diameter (23 to 12 nm), surface area (484.81 to 132.41 $m^2\ g^{-1}$) and pore volume (1.27 to 0.36 cc/g) of MSN after NC growth, which agreed well with TEM results to support the successful crystallization of the perovskites inside the NH_2-MSNs. The crystal structures of the resulting $CsPbBr_3$@MSNs nanocomposites were identified by powder X-ray diffraction patterns (XRD) **(Figure 1e)**. The $CsPbBr_3$@MSNs powder exhibited the typical orthorhombic phase structure of $CsPbBr_3$ (JCPDF #18-0364).[1, 40] Notably, a broad peak derived from amorphous SiO_2 was observed between 20 and 27°.[35, 36] The elemental composition of the powder by XPS revealed all expected elements (Cs3d, C1s, Si2s, N1s, Pb4f, and Br3d) from both $CsPbBr_3$ and NH_2-MSNs **(Figures S5 and S6)**. High resolution XPS analysis corresponding to N1s can be fitted with two peaks at 398 and 400 eV, which were attributed to the N-C and N-Pb coordination, respectively. Those results collectively confirmed the successful loading of $CsPbBr_3$ NCs in the MSN matrices **(Scheme 1)**.

The optical properties of the $CsPbBr_3$@MSNs nanocomposites were characterized by UV-Vis absorption and photoluminescence (PL) spectra. As expected, the nanocomposites showed bright

green fluorescence (inset in **Figure 1f**), a sharp PL maximum peak at 523 nm, and a 62±2.1% PLQY value.

We investigated the catalytic performance of $CsPbBr_3$@MSNs as a photocatalyst (PC) for PET-RAFT polymerization, using methyl methacrylate (MMA) and 2-(*n*-butyltrithiocarbonate) propionic acid (BTPA) as the prototypical monomer and chain transfer agent (CTA), respectively. The polymerization was conducted with various catalyst loadings (0–2.1 wt.%, **Figure S7**) relative to the monomer, and excitation lights (365 nm, 460 nm, visible light, and sun light, 10 mW/cm^2) using toluene as the solvent, as shown in **Table 1 and Figure S8**.

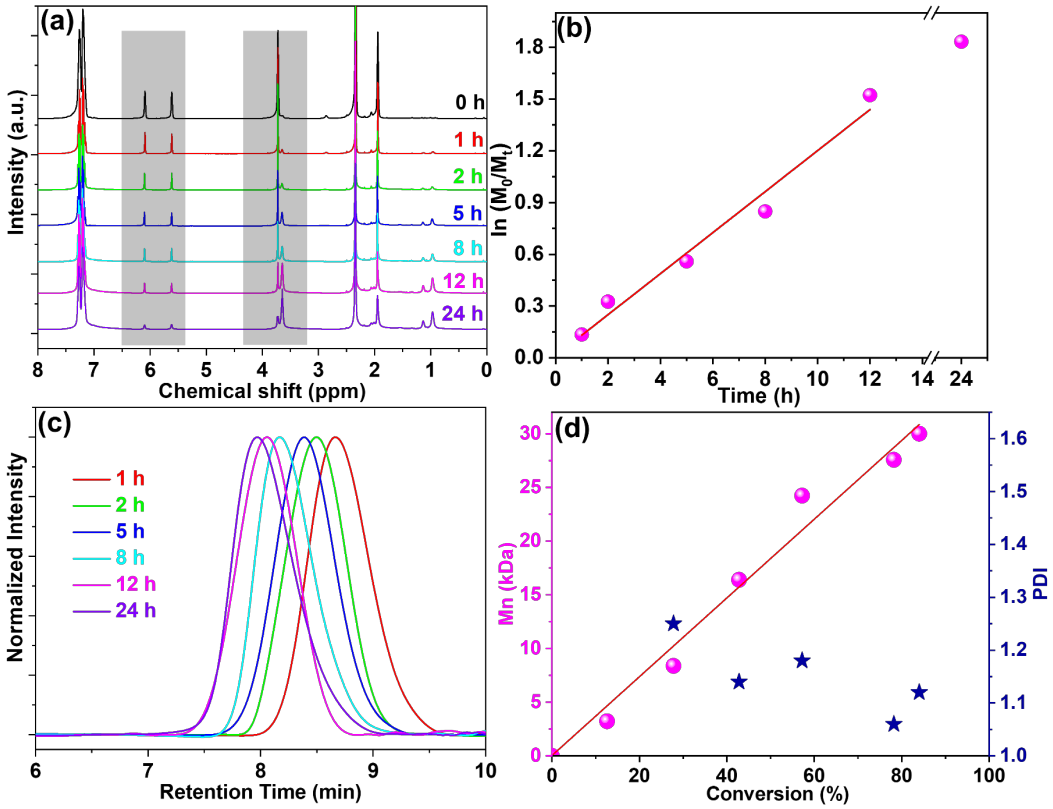

Figure 2. (a) ^{1}H-NMR spectra (solvent: Acetone-d_6) of photopolymerized PMMA over time (7-7.5 ppm: the aromatic peaks from Toluene). (b) MMA monomer conversion kinetics under constant illumination in the presence of $CsPbBr_3$@MSNs PC. (c) GPC profiles of the photopolymerized PMMA over time. (d) Molecular weights and polydispersity (PDI) of the photopolymerized

PMMA against monomer conversion.

It was observed that the fluidity of the reaction mixture decreased and the viscosity increased over time, consistent with polymer formation. To confirm chain end fidelity of the polymers, we purified the PMMA product (see details in Supporting Information) at different time interval and analyzed the chemical structure by ^{1}H-NMR spectroscopy. In the ^{1}H-NMR spectrum of MMA, the chemical shifts observed at 5.5–6.5 ppm and 3.65 ppm were attributed to the double bond and methoxy protons, respectively **(Figures 2a and S11)**. As polymerization occurred, the intensity of both C=C and methoxy protons decreased while a new peak at 3.59 ppm, corresponding to the methoxy groups in PMMA, increased over time. The appearance of resonances of the RAFT agent between 7.5–8.2 ppm further confirmed PMMA formation by RAFT polymerization (**Figures S10–S12**).

Figure 2 shows further details of the time-dependent living polymerization of MMA irradiated at 450 nm using $CsPbBr_3$@MSNs as the photocatalyst. The PMMA was sampled at different polymerization times and characterized by gel permeation chromatography (GPC). The polymerization kinetics was assessed by plotting $\ln([M]_0/[M]_t)$ against time, which showed a first-order kinetic behavior (**Figure 2b**). Although it is difficult to compare the polymerization rate with that of QDs reported due to the different photocatalytic reaction conditions, $CsPbBr_3$@MSNs presented satisfying polymerization rate (0.126 h^{-1}) compared with that of the reported QDs (**Table S1**). [41-44] The MMA monomer conversion exceeded 84% after 24 h irradiation. The corresponding PDI was as low as 1.12, along with a number averaged molecular weight (Mn) of 30 kDa as determined by GPC. **Figure 2c** shows GPC chromatograms of PMMA polymers over time (0−24 h), demonstrating symmetrical unimodal distributions. The correlation plot further demonstrated a linear molecular weight increase with MMA monomer conversion. All results validated the well-

controlled living nature of the RAFT polymerization of MMA under light irradiation.

Control experiments confirmed the impact of each reaction component, including various $CsPbBr_3$@MSNs loadings (or lack thereof), excitation light wavelengths (including dark conditions), monomers, as well as the CTAs **(Table 1)**. No polymerization occurred in the dark or in the absence of $CsPbBr_3$@MSNs, confirming the photocatalytic role of $CsPbBr_3$@MSNs. Under the same irradiation time and wavelength, higher PC loading (from 0.6 to 2.1 wt.%) resulted in higher overall conversion rate and molecular weight **(Table 1)**. In the absence of $CsPbBr_3$@MSNs, polymerization did occur under 365 nm irradiation with 16.1% monomer conversion (Mn=6.0 kDa and PDI=1.41), possibly due to the CTA being photoactivated by UV light. However, the contribution to the polymerization conversion was far below that of $CsPbBr_3$@MSNs.Visible light was the least effective for the polymerization (23.2 %. and 7.8 kDa) while the highest conversion (92.5%, 32.3 kDa) occurred using 365 nm excitation.

Table 1. Summary of polymerization outcomes using $CsPbBr_3$@MSNs catalyst with different monomers, catalyst loadings and light sources.

No.	Monomer [a]	Monomer:CTA	Catalyst (wt%) [b]	Light Sources [c]	Time (h)	Conversion (%) [d]	Mn (kDa) [e]	Mw/Mn (PDI) [e]
0	MMA	250:1	2.1	Dark	24	0	/	/
1	MMA	250:1	2.1	365 nm	24	92.5	32.3	1.13
2	MMA	250:1	0	365 nm	24	16.1	6.0	1.41
3	MMA	250:1	2.1	450 nm	24	84.0	30.0	1.12
4	MMA	250:1	2.1	Visible light	24	23.2	7.8	1.23
5	MMA	250:1	0	450 nm	24	Trace	/	/
6	MMA	250:1	0.6	450 nm	24	38.0	13.3	1.25
7	MMA	250:1	1.2	450 nm	24	52.6	21.5	1.18
8	MMA	250:0	2.1	450 nm	24	18.5	6.7	2.21
9	MMA	250:1	2.1	Sunlight	24	19.8	6.9	1.97
10	Styrene	250:1	2.1	450 nm	24	87.8	30.9	1.15
11	GMA	250:1	2.1	450 nm	24	78.4	31.4	1.21
12	FMA	250:1	2.1	450 nm	24	57.6	25.6	1.32
13	DFHM	250:1	2.1	450 nm	24	24.3	21.8	1.39
14	MA-POSS	250:1	2.1	450 nm	24	19.6	45.7	1.51

[a] GMA: glycidyl Methacrylate; FMA: trifluoroethyl methacrylate; DFHM: dodecafluoheptane methacrylate; MA-POSS: methacrylate polyhedral oligomeric silsesquioxane. [b] Catalyst loadings were calculated relative to

the monomer (Figure S7). [c] Polymerizations performed in dark, under UV-LED (365 nm), blue-LED (460 nm), white-LED (Visible light) and sunlight. [d] Monomer conversion was calculated based on ^{1}H-NMR analysis. [e] Mn and Mw/Mn were determined by GPC.

Furthermore, we expanded the monomer scope to explore the versatility and generality of $CsPbBr_3$@MSNs-based PCs for catalyzing PET-RAFT polymerization. Using $CsPbBr_3$@MSNs as PCs, polymerizations of styrene, glycidyl methacrylate and trifluoroethyl methacrylate monomers occurred readily with 87.8, 78.4 and 57.6 % conversion, respectively, giving rise to polystyrene, polyglycidyl methacrylate and polytrifluoroethyl methacrylate with Mns of 30.9 kDa (PDI of 1.15), 31.4 kDa (PDI of 1.21) and 25.6 ka (PDI of 1.32) **(Table 1 and Figure S13)**. Polymerization of other acrylate monomers such as dodecafluoheptane methacrylate (DFHM) and methacrylate polyhedral oligomeric silsesquioxane (MA-POSS) was also attempted; however, monomer conversion was lower than 25% with polydodecafluoheptane methacrylate of a Mn=21.8 kDa (PDI=1.39), polymethacrylate polyhedral oligomeric silsesquioxane of a Mn=45.7 kDa (PDI=1.51), possibly due to the poor monomer activity and large steric demands. Despite those demanding monomers, successful polymerization of various monomers, low PCs loading, and a wide range of irradiation lights supported $CsPbBr_3$@MSNs as efficient PC for PET-RAFT polymerizations.

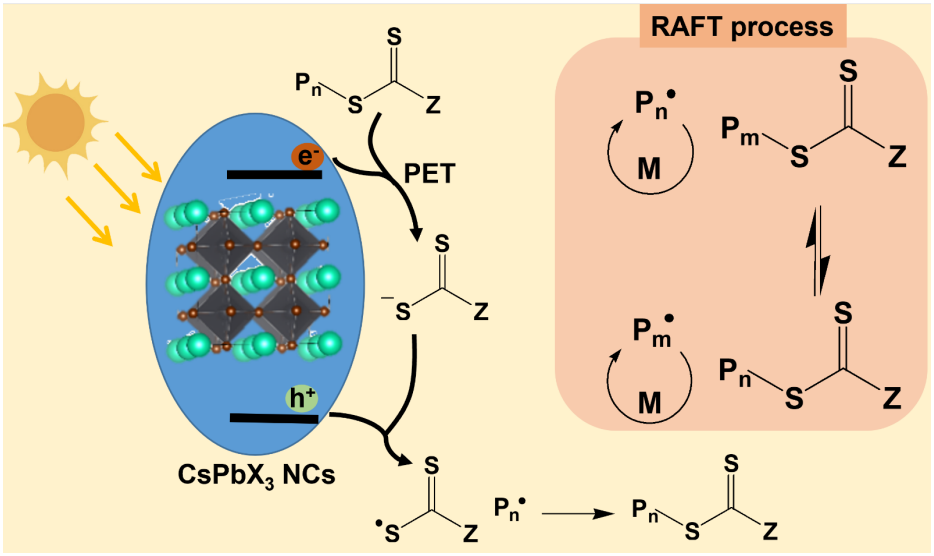

Scheme 2. Proposed mechanism for $CsPbBr_3$@MSNs nanocomposite catalyzed PET-RAFT polymerizations.

To confirm the polymerization mechanism, we studied the fluorescence of $CsPbBr_3$@MSNs nanocomposites while introducing RAFT agents. **Figure S9** shows the PL spectra of $CsPbBr_3$@MSNs nanocomposites with different RAFT agent concentrations. $CsPbBr_3$@MSNs nanocomposite alone featured a strong emission peak at 523 nm. However, introduction of RAFT led to the decrease of the corresponding PL intensity to 57% at 2.5% RAFT loading, and 8% at 10% RAFT loading. The PL quenching effect was ascribed to the transfer of photogenerated carriers from $CsPbBr_3$@MSNs to RAFT agents. This was consistent with the sufficiently negative $CsPbBr_3$ reduction potential (−1.3 V versus SCE) to RAFT agents (–0.3–(–0.8) V versus SCE).[15, 19, 20]

Combining the kinetic studies above and effective PL quenching of $CsPbBr_3$@MSNs by RAFT agent (**Figure S9**), we proposed a photo-induced electron transfer reversible addition-fragmentation chain transfer mechanism to describe photo-polymerization (**Scheme 2**). An excited electron-hole pair initially formed within $CsPbBr_3$@MSN nanocomposites upon excitation with

blue light (450 nm). Facilitated by the matching reductive potentials between $CsPbBr_3$ and the RAFT agent, photoinduced electron transfer (PET) was initiated from the nanocrystal to the RAFT agent to give NC^+, a radical polymer chain, and a reduced thiocarbonate (RAFT agents). The holes in perovskite nanocrystals deactivate the radicals and return to the ground state as part of the catalytic cycle. RAFT living chain growth polymerization were initiated thereafter. [15]

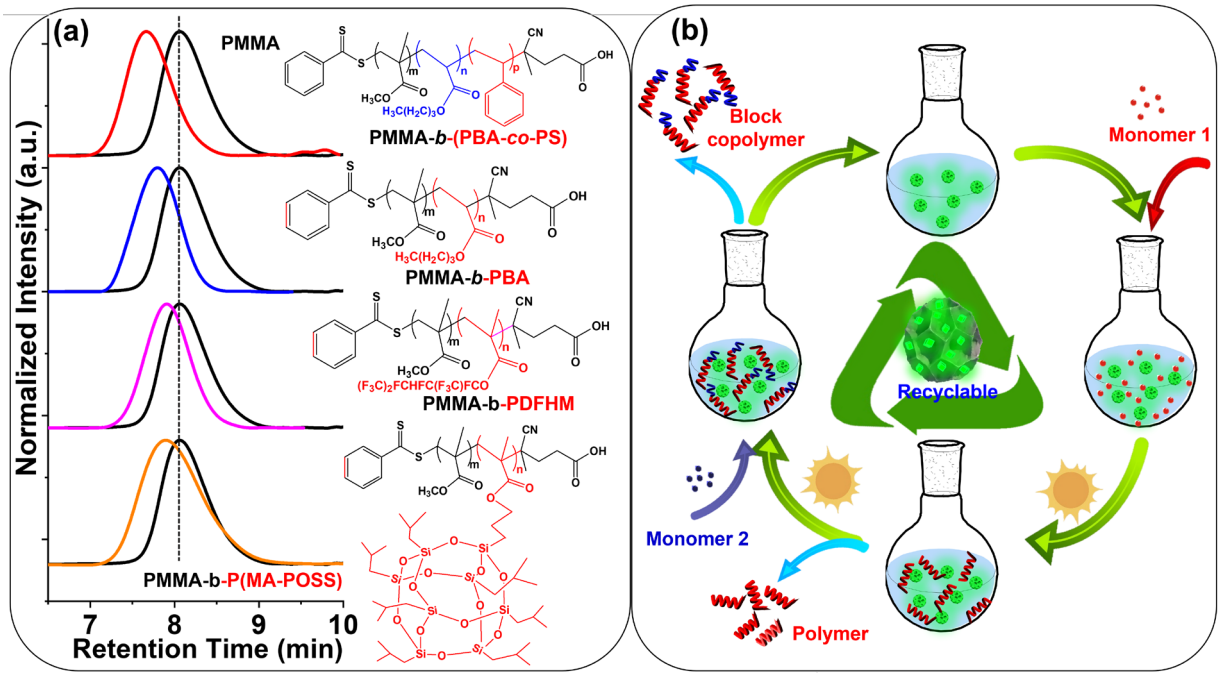

Figure 3. (a) GPC profiles of diblock copolymers from the reaction of PMMA macro chain transfer agents with BA, BA/styrene, DFHM, and MA-POSS. (b) Illustration of the procedures involving the easy separation and recycling of the $CsPbBr_3$@MSNs PCs.

To demonstrate polymerization activity, PMMA (Mn = 16.4 kDa) from the photocatalyzed reaction was used as the macro chain transfer agent to react with styrene, butyl acrylate (BA), dodecafluoheptane methacrylate (DFHM), or POSS-appended methacrylate monomer (MA-POSS) for the synthesis of di-block copolymers **(Figure 3a)**. Copolymers of PMMA-b-PBA, PMMA-b-P(BA-co-PS), PMMA-b-P(MA-POSS), and PMMA-b-PDFHM were successfully obtained using $CsPbBr_3$@MSNs nanocomposites as the PCs, with the chemical structures

characterized by ^{1}H-NMR spectroscopy **(Figures S14-17)**. GPC profiles of all block copolymers clearly indicated chain extension. Compared to the PMMA macroinitiator (Mn=16.4 kDa), the molecular weights of PMMA-b-PBA and PMMA-b-P(BA-co-PS) were increased to 32.2 kDa and 38.6 kDa, respectively, together with a narrow distribution (<1.2), confirming the living character of the PMMA macroinitiator. For reactions with DFHM and MA-POSS monomers, the corresponding PMMA-b-PDFHM and PMMA-b-P(MA-POSS) polymers had lower Mn values (26.5 and 28.3 kDa) and larger molecular weight distributions (1.5-1.8), which were attributed to the low polymerization activity of DFHM and large steric demands/hindrance of MA-POSS.

Traditional photocatalysts would not only contaminate polymers with toxic metal ions, but also lead to polymer degradation.[42] Therefore, a vital aim of this study sought to achieve effective separation between the PCs and the final polymer without losing their successive catalytic efficiencies (**Figure 3b**). As a heterogeneous catalyst, the $CsPbBr_3$@MSNs nanocomposites could be easily separated from the polymerization reaction mixture via centrifugation (**Figures S18 and S19**), and be reused for successive polymerization. Another challenge in employing perovskite-based nanocomposites as PCs is their instability upon exposure to ultraviolet (UV) light, which induces NCs degradation or fusion.[2, 22, 45] By *in-situ* growing $CsPbBr_3$ NCs inside the mesoporous silica nanospheres (MSNs), the ligand-free NCs embedded in the MSNs were spatially confined inside the MSNs and separated by the pore-wall, avoiding potential sintering between NCs under light irradiation (**Figure 4**).[35, 36]

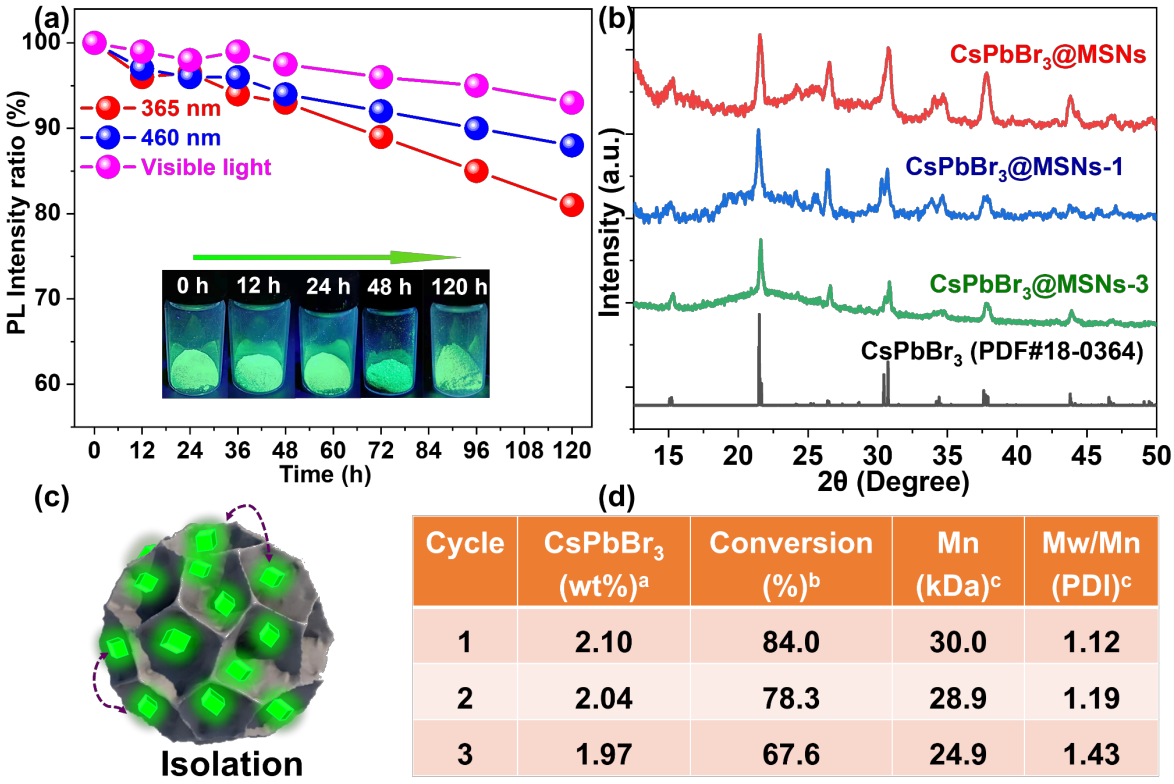

Cycle	$CsPbBr_3$ (wt%)[a]	Conversion (%)[b]	Mn (kDa)[c]	Mw/Mn (PDI)[c]
1	2.10	84.0	30.0	1.12
2	2.04	78.3	28.9	1.19
3	1.97	67.6	24.9	1.43

Figure 4. (a) Relative PLQYs as a function of irradiation time under 365 nm, 460 nm, and visible light. Insets in (a) are the photographs of $CsPbBr_3$@MSNs nanocomposites under 365 nm light over time. (b) Powder X-ray diffraction (PXRD) patterns of $CsPbBr_3$@MSNs nanocomposites before and after three catalytic cycles, and of the standard crystal structure of $CsPbBr_3$. (c) Schematic illustration of $CsPbBr_3$@MSNs composites. (d) Summary of the photocatalytic performance of the $CsPbBr_3$@MSNs PCs for PET-RAFT polymerization for three cycles. (Catalyst loadings were calculated relative to the monomer. [b] Monomer conversion was calculated based on ^{1}H-NMR analysis. [c] Mn and Mw/Mn were determined by GPC.)

The photostability of the $CsPbBr_3$@MSNs nanocomposites was evaluated by measuring the relative PL intensity under continuous light irradiation (365 nm, 460 nm, and visible light) over time (**Figure 4a and S20**). The relative PL intensity of fresh, non-encapsulated $CsPbBr_3$ NCs decreased dramatically, accompanied by a noticeable red-shift and was quenched completely

within 24 h due to the absence of a passivation matrix (**Figure S20**). For the $CsPbBr_3$@MSNs nanocomposites, the relative PL intensity after irradiation at 460 nm maintained 90% of the initial value after 120 h. When irradiated at 365 nm and visible light for 120 h, over 80% and 95% of the initial PL intensities were retained, respectively. The greatly improved stability is consistent with the conceptual design that the perovskite nanocrystals are spatially isolated by the MSN pore-walls, preventing fusion between NCs by heat or light, which has been similarly demonstrated by other encapsulation methods using inorganic or polymer matrixes (**Figure 4c**).[31, 35, 46]

As mentioned, the $CsPbBr_3$@MSNs nanocomposites could be easily separated from the polymerization reaction mixture via centrifugation (**Figures S18 and S19**) and be reused for successive polymerization. After the second cycle polymerization, a slight catalytic efficiency decrease (78.3 % conversion) was observed, resulting in a lower conversion rate with comparable Mn and PDI (**Figure 4d**). A conversion of 67.6 % was observed after the third polymerization cycle, with a PDI of 1.43. PXRD studies revealed that the nanocomposites remained the same crystal structure despite slight decrease of crystallinity after three polymerization cycles (**Figure 4**). Despite the slightly decreased catalytic activity, the demonstrated catalytic conversion and recyclability is superior to other quantum dot based photocatalysts,[42, 43] which again supports the greatly enhanced stability of the $CsPbBr_3$ NCs via MSN encapsulation.

Perovskite-based $CsPbBr_3$@MSNs nanocomposites were prepared and served as efficient PET-RAFT polymerization photocatalysts. The highly luminescent $CsPbBr_3$@MSNs nanocomposites were synthesized in large-scale by growing $CsPbBr_3$ NCs in mesoporous silica nanospheres (MSNs), which yielded $CsPbBr_3$ NCs with a size of ~8.1 nm, and a 62±2.1% PLQY. PET-RAFT polymerizations were successfully achieved using various monomers, excitation lights, and catalyst loadings, to yield polymers with excellent control over dispersity and MWs, as well as

block copolymers with high chain-end fidelity. In addition, the perovskite-based photocatalysts were highly stable to light irradiation. It could be readily separated and purified from the polymerization reaction while retaining high catalytic efficiency, which allowed rapid and effective recycling of the nanocomposites for multiple polymerization cycles. We believe the excellent photocatalytic properties of the perovskite nanocomposites lay the foundation for further exploring their practical applications for polymeric materials synthesis. It is worth noting that, however, there are rooms for further improvement of the photocatalytic performance, such as the environmental stability to humidity, oxygen, and temperature; rational design of effective perovskite-based heterostructures and lead-free perovskites; and exploration of its use in other chemical transformations.

Supporting Information

Materials and chemicals, synthesis approach of MSNs and $CsPbBr_3$@MSNs, photo-polymerization process; stability tests, characterization methods, TEM and SEM images, IR and XPS spectra of MSNs, NH_2-MSNs, and $CsPbBr_3$@MSNs, proposed mechanism for PET-RAFT polymerizations, ^{1}H-NMR spectra of the RAFT and the photopolymerized PMMA, PS, PGMA, PFMA, PMMA-*b*-PBA, PMMA-*b*-(PBA-*co*-PS), PMMA-*b*-PDFHM, PMMA-*b*-P(MA-POSS), optical photograph of the photocatalytic equipment, the catalysts before and after polymerization, relative PL intensity of $CsPbBr_3$ NCs. This material is available free of charge via the Internet at http://pubs.acs.org.

AUTHOR INFORMATION

Corresponding Author

Aizhao Pan − School of Chemistry, Xi'an Jiaotong University, Xianning West Road, 28, Xi'an, 710049, China;

Email: panaizhao2017032@xjtu.edu.cn.

Yanfeng Zhang − School of Chemistry, Xi'an Jiaotong University, Xianning West Road, 28, Xi'an, 710049, China;

Email: yanfengzhang@mail.xjtu.edu.cn.

Yi Liu − The Molecular Foundry and Materials Sciences Division, Lawrence Berkeley National Laboratory, Berkeley, California, 94720, United States.

Email: yliu@lbl.gov

Authors

Chunyu Zhao − School of Chemistry, Xi'an Jiaotong University, Xianning West Road, 28, Xi'an, 710049, China;

Haixia Song − School of Chemistry, Xi'an Jiaotong University, Xianning West Road, 28, Xi'an, 710049, China;

Yinghao Chen − School of Chemistry, Xi'an Jiaotong University, Xianning West Road, 28, Xi'an, 710049, China;

Wei Xiong − School of Chemistry, Xi'an Jiaotong University, Xianning West Road, 28, Xi'an, 710049, China;

Mingyou Hu − School of Chemistry, Xi'an Jiaotong University, Xianning West Road, 28, Xi'an, 710049, China;

Youshen Wu − School of Chemistry, Xi'an Jiaotong University, Xianning West Road, 28, Xi'an, 710049, China;

Ling He − School of Chemistry, Xi'an Jiaotong University, Xianning West Road, 28, Xi'an, 710049, China;

Author Contributions

All authors have given approval to the final version of the manuscript.

Notes

The authors declare no competing financial interest.

ACKNOWLEDGMENT

This work was primarily supported by the National Natural Science Foundation of China (NSFC Grants 52172153, 51802254). Y.L. acknowledges the support from Molecular Foundry, which was supported by the Office of Science, Office of Basic Energy Sciences, of the U.S. Department of Energy under Contract No. DE-AC02-05CH11231. The authors also thank Gang Chang and Jiamei Liu at the Instrument Analysis Center of Xi'an Jiaotong University for their assistance with the TEM and XPS analysis.

REFERENCES

(1) Nedelcu, G.; Protesescu, L.; Yakunin, S.; Bodnarchuk, M. I.; Grotevent, M. J.; Kovalenko, M. V. Fast Anion-Exchange in Highly Luminescent Nanocrystals of Cesium Lead Halide Perovskites ($CsPbX_3$, X = Cl, Br, I). *Nano Lett.* **2015**, *15* (8), 5635-5640.

(2) Dey, A.; Ye, J.; De, A.; Debroye, E.; Ha, S. K.; Bladt, E.; Kshirsagar, A. S.; Wang, Z.; Yin, J.; Wang, Y.; et al. State of the Art and Prospects for Halide Perovskite Nanocrystals. *ACS Nano* **2021**, *15* (7), 10775-10981.

(3) Akkerman, Q. A.; Raino, G.; Kovalenko, M. V.; Manna, L. Genesis, challenges and opportunities for colloidal lead halide perovskite nanocrystals. *Nat. Mater.* **2018**, *17* (5), 394-405.

(4) Pan, A.; He, B.; Fan, X.; Liu, Z.; Urban, J. J.; Alivisatos, A. P.; He, L.; Liu, Y. Insight into the Ligand-Mediated Synthesis of Colloidal $CsPbBr_3$ Perovskite Nanocrystals: The Role of Organic Acid, Base, and Cesium Precursors. *ACS Nano* **2016**, *10* (8), 7943-7954.

(5) Zhang, J. R.; Hodes, G.; Jin, Z. W.; Liu, S. Z. All-Inorganic $CsPbX_3$ Perovskite Solar Cells: Progress and Prospects. *Angew. Chem. Int. Ed.* **2019**, *58* (44), 15596-15618.

(6) Sun, Q. M.; Xu, J. J.; Tao, F. F.; Ye, W.; Zhou, C.; He, J. H.; Lu, J. M. Boosted Inner Surface

Charge Transfer in Perovskite Nanodots@Mesoporous Titania Frameworks for Efficient and Selective Photocatalytic CO_2 Reduction to Methane. *Angew. Chem. Int. Ed.* **2022**, *61* (20), e202200872.

(7) Huang, H. W.; Pradhan, B.; Hofkens, J.; Roeffaers, M. B. J.; Steele, J. A. Solar-Driven Metal Halide Perovskite Photocatalysis: Design, Stability, and Performance. *ACS Energy Lett.* **2020**, *5* (4), 1107-1123.

(8) Zhu, X. L.; Lin, Y. X.; Sun, Y.; Beard, M. C.; Yan, Y. Lead-Halide Perovskites for Photocatalytic alpha-Alkylation of Aldehydes. *J. Am. Chem. Soc.* **2019**, *141* (2), 733-738.

(9) Cardenas-Morcoso, D.; Gualdron-Reyes, A. F.; Vitoreti, A. B. F.; Garcia-Tecedor, M.; Yoon, S. J.; de la Fuente, M. S.; Mora-Sero, I.; Gimenez, S. Photocatalytic and Photoelectrochemical Degradation of Organic Compounds with All-Inorganic Metal Halide Perovskite Quantum Dots. *J. Phys. Chem. Lett.* **2019**, *10* (3), 630-636.

(10) Wang, J.; Liu, J. L.; Du, Z. L.; Li, Z. Q. Recent Advances in Metal Halide Perovskite Photocatalysts: Properties, Synthesis and Applications. *J. Energy. Chem.* **2021**, *54*, 770-785.

(11) Moad, G. Living and Controlled Reversible-Activation Polymerization (RAP) on the Way to Reversible-Deactivation Radical Polymerization (RDRP). *Polym. Int.* **2022,** https://doi.org/10.1002/pi.6424.

(12) Sun, H.; Choi, W.; Zang, N.; Battistella, C.; Thompson, M. P.; Cao, W.; Zhou, X.; Forman, C.; Gianneschi, N. Bioactive Peptide Brush Polymers via Photoinduced Reversible-Deactivation Radical Polymerization, *Angew. Chem. Int. Ed.* **2019**, *131*, 17520-17525.

(13) Fromel, M.; Benetti, E. M.; Pester, C. W. Oxygen Tolerance in Surface-Initiated Reversible Deactivation Radical Polymerizations: Are Polymer Brushes Turning into Technology? *ACS Macro Lett.* **2022**, *11* (4), 415-421.

(14) Liu, D. D.; He, J.; Zhang, L.; Tan, J. B. 100th Anniversary of Macromolecular Science Viewpoint: Heterogenous Reversible Deactivation Radical Polymerization at Room Temperature. Recent Advances and Future Opportunities. *ACS Macro Lett.* **2019**, *8* (12), 1660-1669.

(15) Zhu, Y. F.; Liu, Y. F.; Miller, K. A.; Zhu, H. Y.; Egap, E. Lead Halide Perovskite Nanocrystals as Photocatalysts for PET-RAFT Polymerization under Visible and Near-Infrared Irradiation. *ACS Macro Lett.* **2020**, *9* (5), 725-730.

(16) Xia, Z. N.; Shi, B. F.; Zhu, W. J.; Xiao, Y.; Lu, C. L. Binary Hybridization Strategy toward

Stable Porphyrinic Zr-MOF Encapsulated Perovskites as High-Performance Heterogeneous Photocatalysts for Red to NIR Light-Induced PET-RAFT Polymerization. *Adv. Funct. Mater.* **2022**, 2207655.

(17) Chen, K.; Deng, X. H.; Dodekatos, G.; Tuysuz, H. Photocatalytic Polymerization of 3,4-Ethylenedioxythiophene over Cesium Lead Iodide Perovskite Quantum Dots. *J. Am. Chem. Soc.* **2017**, *139* (35), 12267-12273.

(18) Wong, Y. C.; Ng, J. D.; Tan, Z. K. Perovskite-Initiated Photopolymerization for Singly Dispersed Luminescent Nanocomposites. *Adv. Mater.* **2018**, *30* (21), e1800774.

(19) Ravi, V. K.; Markad, G. B.; Nag, A. Band Edge Energies and Excitonic Transition Probabilities of Colloidal $CsPbX_3$ (X = Cl, Br, I) Perovskite Nanocrystals. *ACS Energy Lett.* **2016**, *1* (4), 665-671.

(20) Xu, J. T.; Jung, K.; Atme, A.; Shanmugam, S.; Boyer, C. A Robust and Versatile Photoinduced Living Polymerization of Conjugated and Unconjugated Monomers and Its Oxygen Tolerance. *J. Am. Chem. Soc.* **2014**, *136* (14), 5508-5519.

(21) Jin, X. Y.; Ma, K. L.; Chakkamalayath, J.; Morsby, J.; Gao, H. F. In Situ Photocatalyzed Polymerization to Stabilize Perovskite Nanocrystals in Protic Solvents. *ACS Energy Lett.* **2022**, *7* (2), 610-616.

(22) Seth, S.; Ahmed, T.; De, A.; Samanta, A. Tackling the Defects, Stability, and Photoluminescence of $CsPbX_3$ Perovskite Nanocrystals. *ACS Energy Lett.* **2019**, *4* (7), 1610-1618.

(23) VanOrman, Z. A.; Weiss, R.; Medina, M.; Nienhaus, L. Scratching the Surface: Passivating Perovskite Nanocrystals for Future Device Integration. *J. Phys. Chem. Lett.* **2022**, *13* (4), 982-990.

(24) Shamsi, J.; Urban, A. S.; Imran, M.; De Trizio, L.; Manna, L. Metal Halide Perovskite Nanocrystals: Synthesis, Post-Synthesis Modifications, and Their Optical Properties. *Chem. Rev.* **2019**, *119* (5), 3296-3348.

(25) Wang, X. C.; Bao, Z.; Chang, Y. C.; Liu, R. S. Perovskite Quantum Dots for Application in High Color Gamut Backlighting Display of Light-Emitting Diodes. *ACS Energy Lett.* **2020**, *5* (11), 3374-3396.

(26) Wang, S. Z.; Amin, A. A. Y.; Wu, L. Z.; Cao, M. H.; Zhang, Q.; Ameri, T. Perovskite Nanocrystals: Synthesis, Stability, and Optoelectronic Applications. *Small Struct.* **2021**, *2* (3),

2000124.

(27) He, Y.; Yoon, Y. J.; Harn, Y. W.; Biesold-McGee, G. V.; Liang, S.; Lin, C. H.; Tsukruk, V. V.; Thadhani, N.; Kang, Z. T.; Lin, Z. Q. Unconventional Route to Dual-Shelled Organolead Halide Perovskite Nanocrystals with Controlled Dimensions, Surface Chemistry, and Stabilities. *Sci. Adv.* **2019**, *5* (11), eaax4424.

(28) Loiudice, A.; Saris, S.; Oveisi, E.; Alexander, D. T. L.; Buonsanti, R. $CsPbBr_3$ QD/AlOx Inorganic Nanocomposites with Exceptional Stability in Water, Light, and Heat. *Angew. Chem. Int. Edit.* **2017**, *56* (36), 10696-10701.

(29) Zhong, Q. X.; Cao, M. H.; Hu, H. C.; Yang, D.; Chen, M.; Li, P. L.; Wu, L. Z.; Zhang, Q. One-Pot Synthesis of Highly Stable $CsPbBr_3$@SiO_2 Core-Shell Nanoparticles. *ACS Nano* **2018**, *12* (8), 8579-8587.

(30) Zhou, Q. C.; Bai, Z. L.; Lu, W. G.; Wang, Y. T.; Zou, B. S.; Zhong, H. Z. In Situ Fabrication of Halide Perovskite Nanocrystal-Embedded Polymer Composite Films with Enhanced Photoluminescence for Display Backlights. *Adv. Mater.* **2016**, *28* (41), 9163-9168.

(31) Hintermayr, V. A.; Lampe, C.; Low, M.; Roemer, J.; Vanderlinden, W.; Gramlich, M.; Bohm, A. X.; Sattler, C.; Nickel, B.; Lohmuller, T.; et al. Polymer Nanoreactors Shield Perovskite Nanocrystals from Degradation. *Nano Lett.* **2019**, *19* (8), 4928-4933.

(32) Zhang, Q. G.; Wang, B.; Zheng, W. L.; Kong, L.; Wan, Q.; Zhang, C. Y.; Li, Z. C.; Cao, X. Y.; Liu, M. M.; Li, L. Ceramic-like Stable $CsPbBr_3$ Nanocrystals Encapsulated in Silica Derived from Molecular Sieve Templates. *Nat. Commun.* **2020**, *11* (1), 31.

(33) Zhang, C. Y.; Li, W. B.; Li, L. Metal Halide Perovskite Nanocrystals in Metal-Organic Framework Host: Not Merely Enhanced Stability. *Angew. Chem. Int. Ed.* **2021**, *60* (14), 7488-7501.

(34) Li, Z. J.; Hofman, E.; Li, J.; Davis, A. H.; Tung, C. H.; Wu, L. Z.; Zheng, W. W. Photoelectrochemically Active and Environmentally Stable $CsPbBr_3$/TiO_2 Core/Shell Nanocrystals. *Adv. Funct. Mater.* **2018**, *28* (1), 1704288.

(35) Dirin, D. N.; Protesescu, L.; Trummer, D.; Kochetygov, I. V.; Yakunin, S.; Krumeich, F.; Stadie, N. P.; Kovalenko, M. V. Harnessing Defect-Tolerance at the Nanoscale: Highly Luminescent Lead Halide Perovskite Nanocrystals in Mesoporous Silica Matrixes. *Nano Lett.* **2016**, *16* (9), 5866-5874.

(36) Pan, A. Z.; Wu, Y. S.; Yan, K.; Yu, Y.; Jurow, M. J.; Ren, B. Y.; Zhang, C.; Ding, S. J.; He, L.;

Liu, Y. Stable Luminous Nanocomposites of Confined Mn^{2+}-Doped Lead Halide Perovskite Nanocrystals in Mesoporous Silica Nanospheres as Orange Fluorophores. *Inorg. Chem.* **2019**, *58* (6), 3950-3958.

(37) Ushakova, E. V.; Cherevkov, S. A.; Sokolova, A. V.; Li, Y. X.; Azizov, R. R.; Baranov, M. A.; Kurdyukov, D. A.; Stovpiaga, E. Y.; Golubev, V. G.; Rogach, A. L.; et al. Stable Luminescent Composite Microspheres Based on Porous Silica with Embedded $CsPbBr_3$ Perovskite Nanocrystals. *Chemnanomat* **2020**, *6* (7), 1080-1085.

(38) Rubino, A.; Calio, L.; Garcia-Bennett, A.; Calvo, M. E.; Miguez, H. Mesoporous Matrices as Hosts for Metal Halide Perovskite Nanocrystals. *Adv. Opt. Mater.* **2020**, *8* (9), 1901868.

(39) Pan, A. Z.; Ma, X.; Huang, S. Y.; Wu, Y. S.; Jia, M. J.; Shi, Y. M.; Liu, Y.; Wangyang, P. H.; He, L.; Liu, Y. $CsPbBr_3$ Perovskite Nanocrystal Grown on MXene Nanosheets for Enhanced Photoelectric Detection and Photocatalytic CO_2 Reduction. *J. Phys. Chem. Lett.* **2019**, *10, 21*, 6590-6597.

(40) Almeida, G.; Goldoni, L.; Akkerman, Q.; Dang, Z.; Khan, A. H.; Marras, S.; Moreels, I.; Manna, L. Role of Acid-Base Equilibria in the Size, Shape, and Phase Control of Cesium Lead Bromide Nanocrystals. *ACS Nano* **2018**, *12* (2), 1704-1711.

(41) Liang, Y. C.; Ma, H. H.; Zhang, W. J.; Cui, Z.; Fu, P.; Liu, M. Y.; Qiao, X. G.; Pang, X. C. Size Effect of Semiconductor Quantum Dots as Photocatalysts for PET-RAFT Polymerization. *Polym. Chem.* **2020**, *11* (31), 4961-4967.

(42) McClelland, K. P.; Clemons, T. D.; Stupp, S. I.; Weiss, E. A. Semiconductor Quantum Dots Are Efficient and Recyclable Photocatalysts for Aqueous PET-RAFT Polymerization. *ACS Macro Lett.* **2020**, *9* (1), 7-13.

(43) Wang, Q.; Hu, L. J.; Cui, Z.; Fu, P.; Liu, M. Y.; Qiao, X. G.; Pang, X. C. Dual Roles of Amino-Functionalized Silicon Quantum Dots (SiQDs) for Visible-Light-Induced Surface-Initiated PET-RAFT Polymerization on Substrates. *ACS Appl. Mater. Inter.* **2020**, *12* (37), 42161-42168.

(44) Jiang, J. J.; Ye, G.; Wang, Z.; Lu, Y. X.; Chen, J.; Matyjaszewski, K. Heteroatom-Doped Carbon Dots (CDs) as a Class of Metal-Free Photocatalysts for PET-RAFT Polymerization under Visible Light and Sunlight. *Angew. Chem. Int. Ed.* **2018**, *57* (37), 12037-12042.

(45) Wu, Y.; Li, X. M.; Zeng, H. B. Highly Luminescent and Stable Halide Perovskite Nanocrystals. *ACS Energy Lett.* **2019**, *4* (3), 673-681.

(46) Avugadda, S. K.; Castelli, A.; Dhanabalan, B.; Fernandez, T.; Silvestri, N.; Collantes, C.;

Baranov, D.; Imran, M.; Manna, L.; Pellegrino, T.; et al. Highly Emitting Perovskite Nanocrystals with 2-Year Stability in Water through an Automated Polymer Encapsulation for Bioimaging. *ACS Nano* **2022**, *16* (9), 13657-13666.